Observing a Berry curvature effect in CH_2OH photodissociation via molecular dynamics simulations

Ming Zhang [1], Xiaoyu Mi,[1] Linfeng Zhang,[1] Chengyin Wu [1,2,3] Haitan Xu,[4,5,6,*] and Zheng Li [1,2,3,†]

[1]*State Key Laboratory for Mesoscopic Physics and Collaborative Innovation Center of Quantum Matter, School of Physics, Peking University, Beijing 100871, China*

[2]*Collaborative Innovation Center of Extreme Optics, Shanxi University, Taiyuan, Shanxi 030006, China*

[3]*Peking University Yangtze Delta Institute of Optoelectronics, Nantong, Jiangsu 226010, China*

[4]*School of Materials Science and Intelligent Engineering, Nanjing University, Suzhou 215163, China*

[5]*Shishan Laboratory, Nanjing University, Suzhou 215163, China*

[6]*School of Physical Sciences, University of Science and Technology of China, Hefei 230026, China*

(Received 4 July 2023; revised 23 January 2024; accepted 19 April 2024; published 6 May 2024)

The Berry curvature of molecular electronic wave function serves as an electron-spin-dependent effective magnetic field, which results in an effective magnetic force that can lead to electron-spin-dependent molecular dynamics. We propose an experimental scheme to observe this Berry curvature effect in molecular dynamics. We show that in CH_2OH photodissociation process, the dissociation rates are different for molecules with opposite electronic spin directions, and the evolution of the electronic density of molecules with opposite spins can be observed with ultrafast x-ray diffraction using free electron lasers, which demonstrates the modified nuclear motion due to the electron-spin-dependent effective magnetic force. Our work paves the way to the direct observation of the Berry curvature effect in molecular systems and chemical reactions, and the Berry curvature effect has profound and wide applications in various areas of physics and chemistry.

DOI: 10.1103/PhysRevB.109.184304

I. INTRODUCTION

Berry curvature is a fundamental property of quantum wave functions [1], and has far-reaching applications in many quantum systems such as topological insulators [2–4] and quantum Hall fluids [5–8]. For molecular systems, the Berry curvature of electronic wave functions can result in an effective magnetic field, which acts on the nuclei as an additional force apart from the gradient force of the potential energy surface (PES) [9–14], and has practical effects in chemical reactions and molecular dynamics [15–19]. The molecules with opposite spins experience opposite effective magnetic fields due to the time-reversal symmetry [20], and the corresponding reaction pathways can be dramatically altered, which leads to electron-spin-dependent nuclear motions in molecular dynamics [17].

Though the presence of the effective magnetic force due to the Berry curvature has been proposed for molecular systems [18], it remains an open problem to observe the corresponding effects in molecular dynamics. Here we propose an experimental scheme to observe the Berry curvature effects by detecting the evolution of electronic spin density. We use ultrafast x-ray diffraction to capture the electronic spin density and thus the nuclear motion modified by the effective magnetic force within the hundreds-femtosecond characteristic time scale of molecular dissociation reaction. Based on *ab initio* ultrafast x-ray diffraction calculation and molecular dynamics simulation, we demonstrate that the nontrivial spin density due to the modified nuclear motion by electron-spin-dependent effective magnetic field can be probed and quantitatively reconstructed with ultrafast x-ray diffraction.

We consider the CH_2OH photodissociation process involving the ground state $|1^2A\rangle$ and the first excited state $|2^2A\rangle$ [21,22], as shown in Fig. 1(a). The dissociation starting from the $|2^2A\rangle$ state is triggered by a linearly polarized ultraviolet (UV) pump pulse of 385 nm [23]. The reaction proceeds in an external magnetic field $\vec{B}$, which aligns the spin along the field axis, which is indispensable to observe the Berry curvature effect. The evolution of the electron spin density in the molecular dissociation process can be observed and reconstructed by circularly polarized x-ray diffraction, as schematically shown in Figs. 1(b) and 1(c).

II. THEORY AND SIMULATION DETAILS

A. Hamiltonian

The Hamiltonian of $CH_2OH \rightarrow H + CH_2O$ nonadiabatic photodissociation process is given by

$$\hat{H} = \hat{H}_0 + \hat{H}_{SO} + \hat{H}_Z, \tag{1}$$

where $\hat{H}_0$ is the molecular Coulomb Hamiltonian including electronic and nuclear kinetic energies and the Coulomb interaction energy. $\hat{H}_{SO}$ is Breit-Pauli form spin-orbit coupling Hamiltonian [19,24]

$$\hat{H}_{SO} = -\frac{\alpha^2}{2}\sum_{i,I}\frac{Z_I}{|\vec{r}_{iI}|^3}(\vec{r}_{iI}\times\vec{p}_i)\cdot\vec{s}_i, \tag{2}$$

*haitanxu@nju.edu.cn
†zheng.li@pku.edu.cn

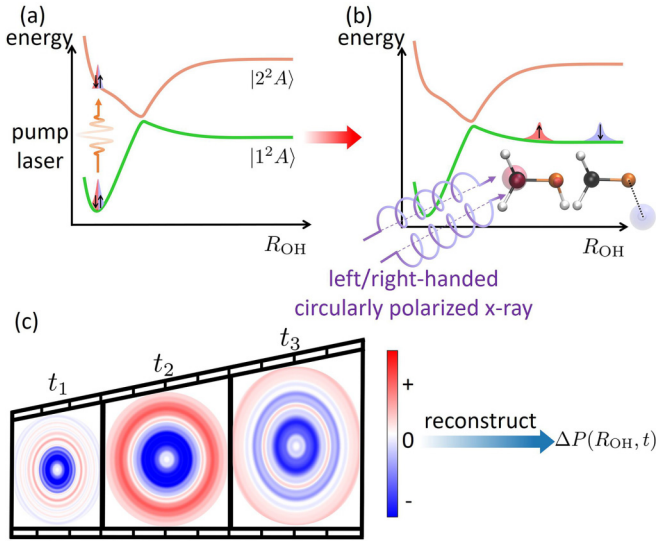

FIG. 1. Schematic of observing the Berry curvature effect in molecular dynamics with circularly polarized ultrafast x-ray diffraction. (a) Initialization of the CH_2OH molecules for dissociation by an ultraviolet (UV) pump laser. (b) Observation of the electron spin density during the dissociation process by circularly polarized x-ray. The Berry curvature effect results in different O–H distance for different electronic spins at the same time during the dissociation. In (a) and (b), the black, orange, and white spheres represent C, O, and H atoms in CH_2OH. The red and blue peaks with arrows represent nuclear wave packets for spin-up and spin-down molecules. (c) The diffraction images corresponding to the difference between scattering intensities using left-handed and right-handed circularly polarized x rays. Red and blue colors represent positive and negative signals. The probability density difference $\Delta P(R_{OH}, t)$ between spin-up and spin-down molecules with O–H distance R_{OH} at time t can be reconstructed from the diffraction images.

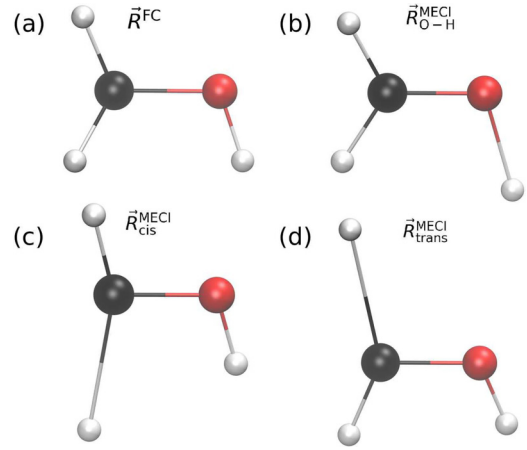

FIG. 2. Representative geometries in CH_2OH dissociation dynamics. The coordinates for these geometries are provided in Ref. [21]. (a) Franck-Condon (FC) geometry $\vec{R}^{FC}$, namely, the equilibrium geometry in the ground state. (b) $\vec{R}^{MECI}_{O-H}$, (c) $\vec{R}^{MECI}_{cis}$ and (d) $\vec{R}^{MECI}_{trans}$ are local minimal energy conical intersections (MECI) between $|1^2A\rangle$ and $|2^2A\rangle$ states. Black, red, and white spheres represent C, O, and H atoms, respectively.

where $\alpha = 1/137$ is the fine-structure constant, Z_I is the atomic number of Ith nucleus, $\vec{p}_i$ and $\vec{s}_i$ are the momentum and spin for the ith electron, $\vec{r}_{iI}$ is the position vector from electron i to nucleus I. Define the direction of external magnetic field to be Z axis in laboratory frame. The Zeeman Hamiltonian under external magnetic field B is

$$\hat{H}_Z = \frac{\alpha}{2} B(\hat{L}_Z + 2\hat{S}_Z), \tag{3}$$

where $\hat{L}_Z$ and $\hat{S}_Z$ are the projections of orbital and spin angular momentum operators along Z axis, respectively.

The spin density signal is nonvanishing only when the initial molecular spin directions are aligned. In the absence of external magnetic field, the total spin separation effect vanishes, because after averaging for all spin polarization directions, the Fourier transformed total spin density is

$$\begin{aligned}\vec{s}_{\text{total}}(\vec{q}) &= \int_{SO(3)} d\mathcal{R}\langle \hat{U}(\mathcal{R})\psi|\hat{\vec{s}}(\vec{q})|\hat{U}(\mathcal{R})\psi\rangle \\ &= \int_{SO(3)} d\mathcal{R}\langle \psi|\hat{U}^\dagger(\mathcal{R})\hat{\vec{s}}(\vec{q})\hat{U}(\mathcal{R})|\psi\rangle \\ &= \int_{SO(3)} d\mathcal{R}\langle \psi|\mathcal{R}\hat{\vec{s}}(\vec{q})|\psi\rangle = 0,\end{aligned} \tag{4}$$

where $\hat{U}(\mathcal{R}(\theta,\vec{n})) = e^{-i\theta\vec{n}\cdot\hat{\vec{\sigma}}/2}$ is the representation of three-dimensional (3D) rotation operator $\mathcal{R}(\theta,\vec{n})$, $\vec{\sigma}$ is the vector of Pauli matrices, $\hat{\vec{s}}(\vec{q})$ is the Fourier transformed spin density operator, which will be defined later in Sec. II D, $\mathcal{R}$ ranges over all possible rotation matrices, and we used the relation of Pauli matrices $\hat{U}^\dagger(\mathcal{R})\hat{\vec{\sigma}}\hat{U}(\mathcal{R}) = \mathcal{R}\hat{\vec{\sigma}}$. Thus, Eq. (4) implies vanishing spin density signal in the absence of external magnetic field. Therefore, the external magnetic field is indispensable to the observation of the net Berry curvature effect. Meanwhile, the external magnetic field should not be too large as the electronic spin density signal from the spin polarized Boltzmann distribution of initial states due to Zeeman energy splitting could interfere with the target spin density signal originating from the Berry curvature effect, which will be discussed in Sec. II B and Sec. III C. Thus we choose a proper external magnetic field strength $B = 0.1$ T.

To estimate of energy scales of spin-orbit coupling and Zeeman interactions, we consider some representative geometries in CH_2OH dissociation dynamics [21], including the Franck-Condon (FC) geometry $\vec{R}^{FC}$, which is the equilibrium geometry in the $|1^2A\rangle$ ground state, and several local minimal energy conical intersections (MECI) between $|1^2A\rangle$ ground state and $|2^2A\rangle$ first excited state. The corresponding molecular structures are shown in Fig. 2. The electronic wave functions are calculated using restricted active space self-consistent field (RASSCF) method [25] with an active space consisting of five electrons and seven orbitals and cc-pVTZ basis set, from which we can calculate the Berry curvature and the ultrafast x-ray diffraction pattern by *ab initio* simulation. As shown in Fig. 3, both $\hat{H}_0$ and $\hat{H}_{SO}$ are time-reversal symmetric and the energy levels remain Kramers degenerate. $\hat{H}_{SO}$ does not induce additional splitting for spin-up and spin-down states. The Zeeman energy splitting ΔE_Z is about 10^{-5} eV, which is much smaller compared to the energy differences between different electronic states.

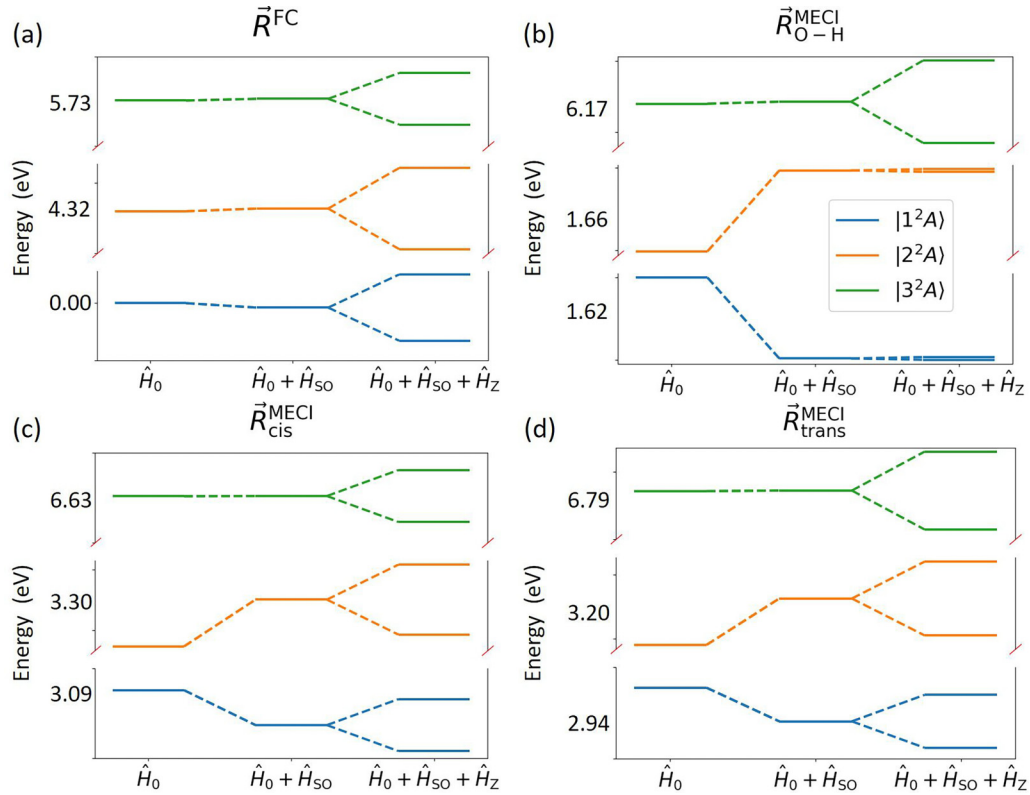

FIG. 3. Energy levels for (a) FC geometry and (b)–(d) representative minimal energy conical intersections (MECI) geometries. Energy eigenvalues for $\hat{H}_0$, $\hat{H}_0+\hat{H}_{\mathrm{SO}}$, and the total Hamiltonian $\hat{H}_0+\hat{H}_{\mathrm{SO}}+\hat{H}_{\mathrm{Z}}$ in Eq. (1) are calculated for each geometry. Notice that the y axis is not continuous for visual convenience of the Zeeman energy splitting ΔE_{Z}, which is about 10^{-5} eV for the magnetic field $B = 0.1$ T.

B. Berry curvature and the effective magnetic force

The Berry curvature for the electron eigenstates $|\psi\rangle$ is given by [26] (in atomic units, au)

$$\Omega_{I\alpha,J\beta}(\psi) = -2\,\mathrm{Im}\langle\nabla_{I\alpha}\psi|\nabla_{J\beta}\psi\rangle, \tag{5}$$

where I and J are the indices of atoms of the molecule, and α and β label the molecular frame axes x, y, z. From Eq. (5), only the imaginary part of $\langle\nabla_{I\alpha}\psi|\nabla_{J\beta}\psi\rangle$ contributes to the Berry curvature. Such complex terms come from both the Pauli matrices in the spin-orbit interaction and the contribution of the magnetic field to the Hamiltonian [27]. The Berry curvature of electronic wave function results in an effective magnetic force $\vec{F}_{\mathrm{B}}$ acting on the nuclei in addition to the gradient force of the electronic PES, given by [15]

$$F_{\mathrm{B},I\alpha} = \sum_{J\beta} v_{J\beta}\Omega_{I\alpha,J\beta}, \tag{6}$$

where $v_{J\beta}$ is the velocity of each nucleus. The PES of CH_2OH, which is the potential energy for the nuclear motion, is *ab initio* calculated as in Ref. [21]. For a system with time-reversal symmetry, the Berry curvature of state $|\psi\rangle$ is opposite for its time-reversal state $|\tilde{\psi}\rangle = \hat{\Theta}|\psi\rangle$, where $\hat{\Theta}$ is the time-reversal operator, because

$$\Omega_{I\alpha,J\beta}(\tilde{\psi}) = -2\,\mathrm{Im}\langle\nabla_{I\alpha}\hat{\Theta}\psi|\nabla_{J\beta}\hat{\Theta}\psi\rangle = -2\,\mathrm{Im}\langle\nabla_{I\alpha}\psi|\nabla_{J\beta}\psi\rangle^* = -\Omega_{I\alpha,J\beta}(\psi), \tag{7}$$

due to the antiunitary property of $\hat{\Theta}$ [20].

We use finite differences method to numerically calculate the Berry curvature in the vicinity of FC and representative MECI geometries [13]

$$\begin{aligned}\Omega_{I\alpha,J\beta}(\psi(\vec{R})) &= -2\,\mathrm{Im}\left\langle \frac{\psi(\vec{R}+\vec{\delta}_{I\alpha})-\psi(\vec{R}-\vec{\delta}_{I\alpha})}{2\delta_{I\alpha}} \middle| \frac{\psi(\vec{R}+\vec{\delta}_{J\beta})-\psi(\vec{R}-\vec{\delta}_{J\beta})}{2\delta_{J\beta}} \right\rangle \\ &= -\frac{1}{2\delta_{I\alpha}\delta_{J\beta}}\,\mathrm{Im}\left(S_{\vec{\delta}_{I\alpha},\vec{\delta}_{J\beta}} - S_{-\vec{\delta}_{I\alpha},\vec{\delta}_{J\beta}} - S_{\vec{\delta}_{I\alpha},-\vec{\delta}_{J\beta}} + S_{-\vec{\delta}_{I\alpha},-\vec{\delta}_{J\beta}}\right),\end{aligned} \tag{8}$$

where $\vec{\delta}_{I\alpha}$ is a small displacement for the Ith atom and αth component of nuclear geometry $\vec{R}$, and $S_{\pm\vec{\delta}_{I\alpha},\pm\vec{\delta}_{J\beta}} = \langle\psi(\vec{R}\pm\vec{\delta}_{I\alpha})|\psi(\vec{R}\pm\vec{\delta}_{J\beta})\rangle$ is the overlap of electronic wave function at different nuclear geometries. We calculate $S_{\pm\vec{\delta}_{I\alpha},\pm\vec{\delta}_{J\beta}}$

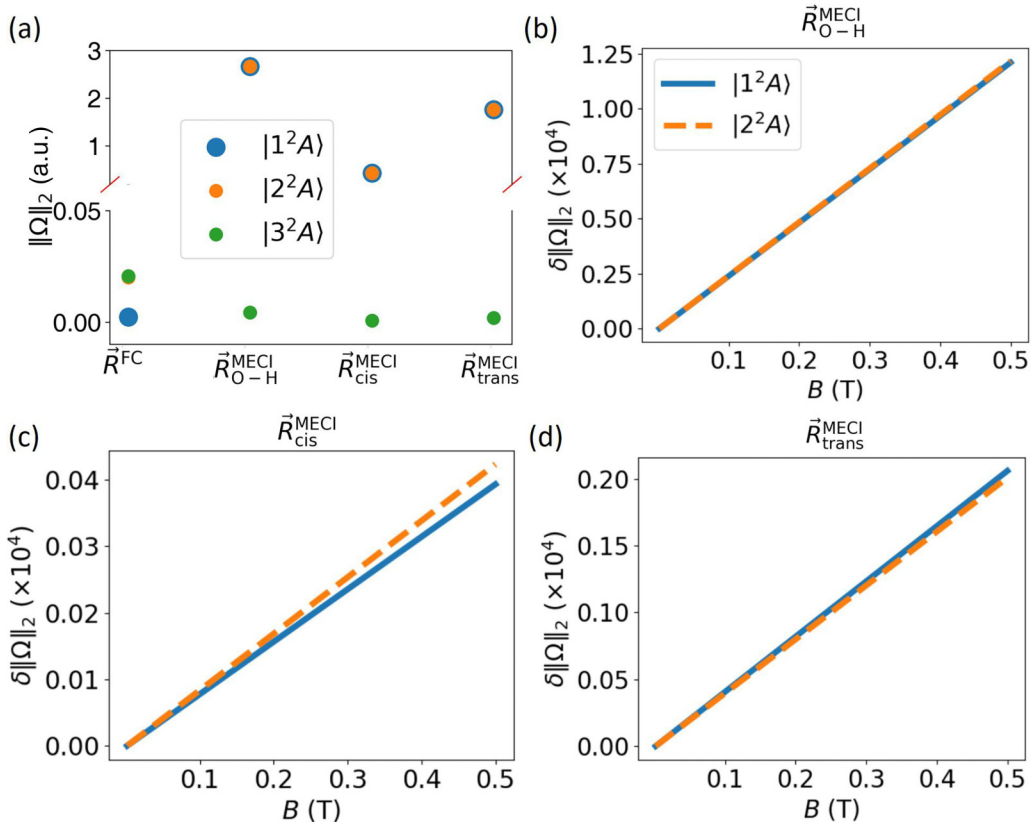

FIG. 4. Berry curvature for FC geometry and the representative MECIs. (a) The 2-norm of Berry curvature $\|\Omega\|_2$ for $\vec{R}^{\rm FC}$ and three representative MECIs between $|1^2A\rangle$ and $|2^2A\rangle$ states in the external magnetic field of 0.1 T. For all three MECIs, the $\|\Omega\|_2$ values of $|1^2A\rangle$ and $|2^2A\rangle$ states are nearly identical. For $\vec{R}^{\rm FC}$ and of $|3^2A\rangle$ state of the MECIs, $\|\Omega\|_2 < 0.005$ a.u. (b)–(d) The change of $\delta\|\Omega\|_2$ [defined in Eq. (9)] with external magnetic field B for $\vec{R}^{\rm MECI}_{\rm O-H}$, $\vec{R}^{\rm MECI}_{\rm cis}$, and $\vec{R}^{\rm MECI}_{\rm trans}$, respectively. When B approaches zero, the Berry curvatures are nearly opposite for the pair of almost time-reversal degenerate states, so $\delta\|\Omega\|_2$ approaches zero. When $B = 0.1$ T, Berry curvatures for the pair of nearly time-reversal degenerate states, which are split by Zeeman energy, are also almost opposite within 0.01% relative difference. The minimal external magnetic field for (b)–(d) is 0.002 T.

using MOLCAS package [28] on the same calculation level RASSCF(5,7)/cc-pvtz.

The Berry curvature effects can be significantly enhanced due to nonadiabatic coupling [17]. The numerical results for the 2-norm of Berry curvature $\|\Omega\|_2$ for $\vec{R}^{\rm FC}$ and representative MECIs $\vec{R}^{\rm MECI}_{\rm O-H}$, $\vec{R}^{\rm MECI}_{\rm cis}$, and $\vec{R}^{\rm MECI}_{\rm trans}$ are shown in Fig. 4. For all the three MECIs between $|1^2A\rangle$ and $|2^2A\rangle$ states, the $\|\Omega\|_2$ value for the nonadiabatically coupled $|1^2A\rangle$ and $|2^2A\rangle$ states are much larger compared to that of $|3^2A\rangle$ state and $\vec{R}^{\rm FC}$ geometry. In the existence of external magnetic field, time-reversal degenerate states are split by Zeeman energy. However, as shown in Fig. 4, Berry curvatures for the pair of states $|\psi\rangle$ and $|\tilde{\psi}\rangle$ are almost opposite. The deviation caused by external magnetic field can be estimated by the relative difference

$$\delta\|\Omega\|_2 = \frac{\|\Omega(\tilde{\psi})\|_2 - \|\Omega(\psi)\|_2}{\|\Omega(\psi)\|_2} < 10^{-4}, \tag{9}$$

when $B = 0.1$ T for all three MECIs shown in Fig. 4. Therefore, the external magnetic field has negligible effect to modify the intrinsic Berry curvature of electronic wave function of molecules. The time-reversal symmetry is not severely broken in the external magnetic field of 0.1 T, so the nearly degenerate time-reversal eigenstates with opposite spin directions in the external magnetic field will experience almost opposite effective magnetic fields caused by the Berry curvature effect of electronic wave function.

C. Molecular dynamics simulation

The molecular dynamics (MD) simulation is carried out based on a multistate PES [21] using modified fewest-switches surface hopping (FSSH) method [29]. The electronic wave function is expanded in the direct product state of spatial state $|\phi_k\rangle$ at given nuclear geometry $\vec{R}(t)$ and spin state $|s\rangle$ ($s = \uparrow, \downarrow$) as

$$|\psi(t)\rangle = \sum_{k,s} c_{k,s}(t)|\phi_k, s\rangle, \tag{10}$$

where $c_{k,s}(t)$ is the expansion coefficient. The electronic wave function is propagated by Schrödinger equation as in standard FSSH algorithm

$$\dot{c}_{k,s} = -i\sum_{j,s'}\langle\phi_k, s|\hat{H}_{\rm el}|\phi_j, s'\rangle c_{j,s'} - \sum_j \vec{v}\cdot\langle\phi_k|\nabla|\phi_j\rangle c_{j,s}, \tag{11}$$

where $\hat{H}_{\rm el}$ is the electronic Hamiltonian including adiabatic potential, $\hat{H}_{\rm SO}$ and $\hat{H}_{\rm Z}$ in Eq. (1), $\vec{v}$ is the nuclear velocity and $\langle\phi_k|\nabla|\phi_j\rangle$ is the derivative coupling operator. Equivalently, the electronic state can be propagated in the adiabatic state representation, where the matrix element of $\hat{H}_{\rm el}$ is diagonalized. The nuclear degrees of freedom are classically propagated along one active adiabatic state [13] denoted as $|\psi_\lambda\rangle$ by

$$\dot{\vec{p}} = -\nabla E_\lambda + \vec{F}_{\rm B} + \vec{F}_{\rm L}, \tag{12}$$

where $\vec{p}$ is the momentum of nuclei, E_λ and $\vec{F}_{\rm B}$ are energy and the effective magnetic force of $|\psi_\lambda\rangle$ state, respectively. $\vec{F}_{\rm L}$ is the Lorentz force and $\vec{F}_{{\rm L},I} = Z_I\vec{v}_I \times \vec{B}$ for the Ith nucleus where Z_I is the atomic number and $\vec{B}$ is the external magnetic field.

In the proximity of conical intersection, the Born-Oppenheimer approximation breaks down and nonadiabatic coupling effect related to electronic state transitions is significant. The surface hopping in the FSSH algorithm corresponds to the nonadiabatic transition between electronic states. For each time step in the FSSH algorithm, the active state $|\psi_\lambda\rangle$ of the trajectory will hop to another state $|\psi_{\lambda'}\rangle$ with a transition probability of [29,30]

$$g_{\lambda\to\lambda'} = \max\left[2\,{\rm Re}\left(\vec{v}\cdot\langle\psi_\lambda|\nabla|\psi_{\lambda'}\rangle\frac{\rho_{\lambda'\lambda}}{\rho_{\lambda\lambda}}\right)\Delta t, 0\right], \tag{13}$$

where $\rho_{\lambda'\lambda}$ is the electronic state reduced density matrix element and Δt is the time interval in MD. For the molecular dynamics simulations of CH_2OH, we use the multistate PES and derivative coupling that were established in Ref. [21]. Briefly, for a series of chosen nuclear geometries, the energies, energy gradients, and derivative coupling vectors are *ab initio* calculated, and symmetry adapted polynomial basis functions are used to construct the analytical forms of PES. The Lorentz force arising from the external magnetic field $B = 0.1$ T is much smaller compared to the effective magnetic force caused by the Berry curvature effect because

$$\frac{|\vec{F}_{\rm L}|}{|\vec{F}_{\rm B}|} \approx \frac{|q\alpha\vec{v}\times\vec{B}|}{\|\Omega\|_2|\vec{v}|} \approx \frac{q\alpha B}{\|\Omega\|_2} \approx \frac{1/137\times 0.1/1720\,{\rm au}}{1\,{\rm au}} \approx 4\times10^{-7}, \tag{14}$$

and also much smaller than the gradient of PES

$$\frac{|\vec{F}_{\rm L}|}{|\nabla V|} \approx \frac{q\alpha vB}{|\nabla V|} \approx \frac{1/137\times10^{-3}\times0.1/1720\,{\rm au}}{0.1\,{\rm au}} \approx 4\times10^{-9}, \tag{15}$$

so $\vec{F}_{\rm L}$ can be ignored in MD. The initial conditions of nuclear geometries and velocities of all MD trajectories are sampled from Wigner distribution, taking into account the vibrational excitations in the 2^2A excited electronic state.

To guarantee that the spin-dependent MD results originate exclusively from the Berry curvature effect, all the MD parameters, including the phase space initial conditions and the random number seed for surface hopping simulation of each pair of spin-up and spin-down trajectories, are identical.

D. Magnetic x-ray scattering circular dichroism cross section

To observe the electron-spin-dependent nuclear wave packet motion due to the Berry curvature effect, we use the circularly polarized ultrafast x-ray diffraction to monitor the evolution of the electron spin density. In this section, we present the formulas of ultrafast nonresonant magnetic x-ray scattering (MXS) circular dichroism (CD) cross section [31–34], i.e., the difference between the scattering intensities with left- and right-handed circularly polarized x rays. The interaction Hamiltonian between target molecules and incident x ray is [31,32]

$$\hat{H}_{\rm int} = \sum_j \frac{\alpha^2}{2}\vec{A}(\vec{r}_j)^2 - \alpha\vec{A}(\vec{r}_j)\cdot\hat{\vec{p}}_j - \alpha\hat{\vec{s}}_j\cdot[\nabla\times\vec{A}(\vec{r}_j)] - \frac{\alpha^3}{2}\hat{\vec{s}}_j\cdot[\dot{\vec{A}}(\vec{r}_j)\times\vec{A}(\vec{r}_j)], \tag{16}$$

where $\vec{r}_j$, $\hat{\vec{p}}_j$, and $\hat{\vec{s}}_j$ are the position, momentum, and spin vectors of the jth electron, $\vec{A}(\vec{r})$ is the vector potential of incident x ray. Although the external magnetic field $B = 0.1$ T could also contribute to the vector potential $\vec{A}(\vec{r})$, it corresponds to the intensity (in SI units)

$$I = \tfrac{1}{2}c\epsilon_0(cB)^2 \approx 1.2\times10^8\,{\rm W/cm^2}, \tag{17}$$

which is much weaker compared to incident x ray and can be ignored. The differential cross section $\frac{d\sigma}{d\Omega}(\vec{q})$ from initial state $|\psi_i\rangle$ to final state $|\psi_f\rangle$ for x-ray scattering including magnetic scattering term can be derived using Kramers-Heisenberg formula [31,33,35] as

$$\frac{d\sigma}{d\Omega}(\vec{q}) = \alpha^4\left|\langle\psi_f|\sum_j e^{i\vec{q}\cdot\vec{r}_j}|\psi_i\rangle(\vec{e}_1\cdot\vec{e}_2^{\,*}) - i\alpha^2\langle\psi_f|\times\sum_j e^{i\vec{q}\cdot\vec{r}_j}(\vec{p}_{j'}\cdot\vec{C}+\vec{\sigma}_{j'}\cdot\vec{D})|\psi_i\rangle\right|^2, \tag{18}$$

where $\vec{e}_1$ and $\vec{e}_2$ are the polarization vectors of incident and outgoing x ray, $\vec{q}$ is momentum transfer of scattered photon, α^4 corresponds to the cross section of about 0.08 barn [36]. The polarization factors $\vec{C}$ and $\vec{D}$ are

$$\vec{C} = \frac{i}{\alpha}(\hat{K}_2-\hat{K}_1)\times(\vec{e}_2^{\,*}\times\vec{e}_1),$$
$$\vec{D} = \frac{\omega}{2}[\vec{e}_2^{\,*}\times\vec{e}_1 - (\hat{K}_2\times\vec{e}_2^{\,*})\times(\hat{K}_1\times\vec{e}_1) - (\vec{e}_2^{\,*}\cdot\hat{K}_1)(\hat{K}_1\times\vec{e}_1) + (\vec{e}_1\cdot\hat{K}_2)(\hat{K}_2\times\vec{e}_2^{\,*})], \tag{19}$$

where $\hat{K}_1$ and $\hat{K}_2$ are the unit length wave vector of incident and outgoing x ray, ω is the x-ray photon frequency. The first term in Eq. (18) is charge scattering cross section, which reflects charge density distribution of the target molecules. The second term in Eq. (18) represents magnetic x-ray scattering signal originated from the interaction between magnetic field of incident x ray and orbital and spin magnetic dipole moments of the molecule. In our calculation, the energy of x-ray photon of wavelength $\lambda = 0.5$ Å is approximately 2.5×10^4 eV, which is much larger compared to the energy level difference of electronic states, which is generally less than 10 eV. The orbital part scattering signal is much smaller than

the spin part, because the polarization factor $\vec{D}$ is proportional to ω.

To eliminate the contribution of strong charge scattering background, consider the circular dichroism signal $\Delta\frac{d\sigma(\vec{q})}{d\Omega}$ [31,34],

$$\Delta\frac{d\sigma(\vec{q})}{d\Omega} = \frac{d\sigma_{\mathrm{L}}(\vec{q})}{d\Omega} - \frac{d\sigma_{\mathrm{R}}(\vec{q})}{d\Omega} = \alpha^6\,\mathrm{Re}[\langle\psi|\hat{\vec{s}}(\vec{q})|\psi\rangle\cdot\vec{D}(\vec{q})], \tag{20}$$

where the subscripts L and R represents left- and right-handed circularly polarized incident x rays, respectively, $\hat{\vec{s}}(\vec{q}) = \sum_{jj'} e^{-i\vec{q}\cdot(\vec{r}_j-\vec{r}_{j'})}\hat{\vec{\sigma}}_{j'}$ is the Fourier transformed spin density operator. The incident x ray is along Z axis in laboratory frame, and the polarization vectors for left- and right-handed circularly polarized incident x rays are $\vec{e}_{1\mathrm{L}} = \frac{\sqrt{2}}{2}(1, i, 0)^T$ and $\vec{e}_{1\mathrm{R}} = \frac{\sqrt{2}}{2}(1, -i, 0)^T$, and then polarization factor $\vec{D}(\vec{q})$ is

$$\vec{D}(\vec{q}) = -2i(\vec{e}^{\,*}_{1\mathrm{L}}\cdot\vec{e}_{2\mathrm{L}})\vec{D}_{\mathrm{L}} + 2i(\vec{e}^{\,*}_{1\mathrm{R}}\cdot\vec{e}_{2\mathrm{R}})\vec{D}_R = -\omega\begin{pmatrix}\cos\phi\sin^3\theta\\ \sin\phi\sin^3\theta\\ \sin^2\theta(1+\cos\theta)\end{pmatrix}. \tag{21}$$

We rewrite the notation of the initial state $|\psi_i\rangle$ as $|\psi\rangle$ for the sake of generality, and summed over all final states $|\psi_f\rangle$, because the ultrafast x-ray scattering signal could cover the final states within the spectral bandwidth of incident ultrashort x-ray pulse [37,38].

The Fourier transformed spin density of state $|\psi\rangle$ is

$$\langle\psi|\hat{\vec{s}}(\vec{q})|\psi\rangle = \langle\psi|\sum_j\hat{\vec{\sigma}}_j|\psi\rangle + \frac{1}{2}\langle\psi|\sum_{j\neq j'}e^{-i\vec{q}\cdot(\vec{r}_j-\vec{r}_{j'})}\hat{\vec{\sigma}}_{j'} + e^{-i\vec{q}\cdot(\vec{r}_{j'}-\vec{r}_j)}\hat{\vec{\sigma}}_j|\psi\rangle$$
$$= \int d\vec{x}_1\hat{\vec{\sigma}}_1\gamma(\vec{x}_1^{\,'},\vec{x}_1)\Big|_{\vec{x}_1^{\,'}=\vec{x}_1} + \int d\vec{x}_1 d\vec{x}_2\left(e^{-i\vec{q}\cdot\vec{r}_{12}}\hat{\vec{\sigma}}_2 + e^{-i\vec{q}\cdot\vec{r}_{21}}\hat{\vec{\sigma}}_1\right)\Gamma(\vec{x}_1^{\,'},\vec{x}_2^{\,'},\vec{x}_1,\vec{x}_2)\Big|_{\vec{x}_1^{\,'}=\vec{x}_1,\vec{x}_2^{\,'}=\vec{x}_2}, \tag{22}$$

where $\vec{x} = (\vec{r}, s)$ includes spatial and spin coordinates, $\gamma(\vec{x}_1^{\,'},\vec{x}_1)$ and $\Gamma(\vec{x}_1^{\,'},\vec{x}_2^{\,'},\vec{x}_1,\vec{x}_2)$ are the one- and two-particle reduced density matrices, respectively. In Eq. (22), the operators with subscripts 1 and 2 first act on the unprimed coordinates $\vec{x}_1$ and $\vec{x}_2$, then the spin density is obtained by taking $\vec{x}_1^{\,'} = \vec{x}_1$ and $\vec{x}_2^{\,'} = \vec{x}_2$. In molecular orbital (MO) basis, the reduced density matrices can be expanded as [39,40]

$$\gamma(\vec{x}_1^{\,'},\vec{x}_1) = \sum_{kl}\gamma_{lk}\varphi_k^*(\vec{x}_1^{\,'})\varphi_l(\vec{x}_1), \tag{23}$$

$$\Gamma(\vec{x}_1^{\,'},\vec{x}_2^{\,'},\vec{x}_1,\vec{x}_2) = \sum_{klmn}\Gamma_{mnkl}\varphi_k^*(\vec{x}_1^{\,'})\varphi_l^*(\vec{x}_2^{\,'})\varphi_m(\vec{x}_1)\varphi_n(\vec{x}_2), \tag{24}$$

where $\varphi_k(\vec{x}) = \varphi_{k_r}(\vec{r})\chi_{k_s}(s)$ is the kth MO with spatial component $\varphi_{k_r}(\vec{r})$ and spin component $\chi_{k_s}(s)$. The integral of MOs are calculated by

$$\int d\vec{x}_1\varphi_k^*(\vec{x}_1)\hat{\vec{\sigma}}_1\varphi_l(\vec{x}_1) = \delta_{k_r l_r}\int d\vec{s}_1\chi_{k_s}^*(s_1)\hat{\vec{\sigma}}_1\chi_{l_s}(s_1), \tag{25}$$

and

$$\int d\vec{x}_1 d\vec{x}_2\varphi_k^*(\vec{x}_1)\varphi_l^*(\vec{x}_2)\left(e^{-i\vec{q}\cdot\vec{r}_{12}}\hat{\vec{\sigma}}_2 + e^{-i\vec{q}\cdot\vec{r}_{21}}\hat{\vec{\sigma}}_1\right)\varphi_m(\vec{x}_1)\varphi_n(\vec{x}_2)$$
$$= \int d\vec{r}_1 d\vec{r}_2\varphi_{k_r}^*(\vec{r}_1)\varphi_{l_r}^*(\vec{r}_2)e^{-i\vec{q}\cdot\vec{r}_{12}}\varphi_{m_r}(\vec{r}_1)\varphi_{n_r}(\vec{r}_2)\times\delta_{k_s m_s}\int d\vec{s}_2\chi_{l_s}^*(s_2)\hat{\vec{\sigma}}_2\chi_{n_s}(s_2)$$
$$+ \int d\vec{r}_1 d\vec{r}_2\varphi_{k_r}^*(\vec{r}_1)\varphi_{l_r}^*(\vec{r}_2)e^{-i\vec{q}\cdot\vec{r}_{21}}\varphi_{m_r}(\vec{r}_1)\varphi_{n_r}(\vec{r}_2)\times\int d\vec{s}_1\chi_{k_s}^*(s_1)\hat{\vec{\sigma}}_1\chi_{m_s}(s_1)\delta_{l_s n_s}. \tag{26}$$

In the simulation of MXS CD signal, the one- and two-particle reduced density matrices γ_{lk} and $\Gamma_{ll'kk'}$, as well as the MO integrals are *ab initio* calculated.

E. Magnetic x-ray scattering signal in the dissociation limit

In this section, we elaborate the analytical model for the MXS CD signal, which we established for the purpose of retrieving the spatial spin density evolution in the ultrafast photodissociation dynamics of CH_2OH. The model is analogous to the independent atom model (IAM) in the theory of molecular diffraction [41]. Because the magnetic field is along Z axis of laboratory frame, we only consider the Z component of spin density, and the first term of Eq. (22) is

$$\int d\vec{x}_1\hat{\sigma}_{1,Z}\gamma(\vec{x}_1^{\,'},\vec{x}_1)\big|_{\vec{x}_1^{\,'}=\vec{x}_1} = \int d\vec{r}_1[\rho(\vec{r}_1\uparrow) - \rho(\vec{r}_1\downarrow)] = \int d\vec{r}\,s_Z(\vec{r}), \tag{27}$$

where $\rho(\vec{r}\uparrow)$ and $\rho(\vec{r}\downarrow)$ are spin-up and spin-down electron densities, respectively, $s_Z(\vec{r}) = \rho(\vec{r}\uparrow) - \rho(\vec{r}\downarrow)$ is the spin density and $\rho(\vec{r}) = \rho(\vec{r}\uparrow) + \rho(\vec{r}\downarrow)$ is the total electron

density. The term of two-particle reduced density matrix is

$$\begin{aligned}
&\int d\vec{x}_1 d\vec{x}_2 e^{-i\vec{q}\cdot\vec{r}_{12}} \hat{\sigma}_{2,Z} \Gamma(\vec{x}_1^{'}, \vec{x}_2^{'}, \vec{x}_1, \vec{x}_2)\big|_{\vec{x}_1^{'}=\vec{x}_1, \vec{x}_2^{'}=\vec{x}_2} \\
&= \int d\vec{r}_1 d\vec{r}_2 e^{-i\vec{q}\cdot\vec{r}_{12}} [\rho^{(2)}(\vec{r}_1\uparrow, \vec{r}_2\uparrow) + \rho^{(2)}(\vec{r}_1\downarrow, \vec{r}_2\uparrow) \\
&\quad - \rho^{(2)}(\vec{r}_1\uparrow, \vec{r}_2\downarrow) - \rho^{(2)}(\vec{r}_1\downarrow, \vec{r}_2\downarrow)] \\
&= \frac{N-1}{2N} \int d\vec{r}_1 d\vec{r}_2 e^{-i\vec{q}\cdot\vec{r}_{12}} [\rho(\vec{r}_1\uparrow) \\
&\quad + \rho(\vec{r}_1\downarrow)][\rho(\vec{r}_2\uparrow) - \rho(\vec{r}_2\downarrow)] \\
&= \frac{N-1}{2N} \int d\vec{r}_1 d\vec{r}_2 e^{-i\vec{q}\cdot\vec{r}_{12}} \rho(\vec{r}_1) s_Z(\vec{r}_2), \qquad (28)
\end{aligned}$$

where we neglected the electronic correlation effects and suppose that $\rho^{(2)}(\vec{x}_1, \vec{x}_2) = \frac{N-1}{2N}\rho(\vec{x}_1)\rho(\vec{x}_2)$, and N is the number of electrons. Thus, the Fourier transformed spin density of the state $|\psi\rangle$ is

$$\begin{aligned}
s_Z(\vec{q}) &= \langle\psi|\hat{s}_Z(\vec{q})|\psi\rangle \\
&= \int d\vec{r} s_Z(\vec{r}) + \frac{N-1}{2N} \int d\vec{r}_1 d\vec{r}_2 [e^{-i\vec{q}\cdot\vec{r}_{12}} \rho(\vec{r}_1) s_Z(\vec{r}_2) \\
&\quad + e^{-i\vec{q}\cdot\vec{r}_{21}} s_Z(\vec{r}_1)\rho(\vec{r}_2)] \\
&= \int d\vec{r} s_Z(\vec{r}) + \frac{N-1}{N} \int d\vec{r}_1 d\vec{r}_2 e^{-i\vec{q}\cdot\vec{r}_{21}} s_Z(\vec{r}_1)\rho(\vec{r}_2). \\
&\qquad (29)
\end{aligned}$$

Figure 5 shows the change of spin density s_H of the H atom with O–H distance R_{OH}. The Mulliken population analysis of spin density is *ab initio* calculated using MOLPRO package [42] on the RASSCF(5,7)/cc-pvtz level. In the dissociation of CH_2OH, when $R_{OH} > 2$ Å, $s_H \approx 1$ and the spin density is completely localized on the dissociated H atom. We assume the spin density to be spherical symmetric

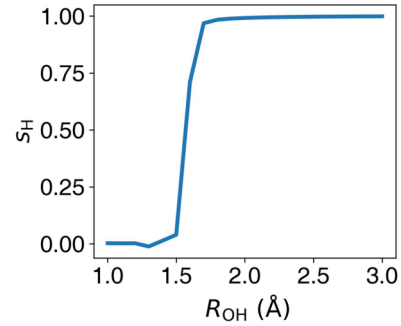

FIG. 5. The change of spin density of dissociated H atom s_H with O–H distance R_{OH} obtained by Mulliken population analysis. Around equilibrium geometry in the ground state, the spin density is mainly distributed on C atom. When $R_{OH} > 2$ Å, spin density is almost completely localized on the dissociated H atom with s_H approaching 1.

$$s_Z(\vec{r}) = \pm\rho_H(|\vec{r} - \vec{r}_H|), \qquad (30)$$

where positive and negative sign corresponds to spin-up and spin-down molecules, respectively. The total electron density is contributed from both CH_2O and the dissociated H atom

$$\rho(\vec{r}) = \rho_X(|\vec{r} - \vec{r}_X|) + \rho_H(|\vec{r} - \vec{r}_H|), \qquad (31)$$

where X represents the CH_2O, which is regarded as a pseudoatom in the model, so Eq. (29) can be expressed as

$$\begin{aligned}
s_Z(\vec{q}) &= \pm N_{un} \pm \frac{N-1}{N} e^{i\vec{q}\cdot\vec{r}_H} \int d\vec{r}_1 e^{i\vec{q}\cdot\vec{r}_1} \rho_H(r_1) \left[e^{-i\vec{q}\cdot\vec{r}_X} \int d\vec{r}_2 e^{-i\vec{q}\cdot\vec{r}_2} \rho_X(r_2) + e^{-i\vec{q}\cdot\vec{r}_H} \int d\vec{r}_2 e^{-i\vec{q}\cdot\vec{r}_2} \rho_H(r_2) \right] \\
&= \pm N_{un} \pm \frac{N-1}{N} \left[f_H^2(q) + e^{i\vec{q}\cdot(\vec{r}_H - \vec{r}_X)} f_H(q) f_X(q) \right], \qquad (32)
\end{aligned}$$

where N_{un} is the number of unpaired electrons in CH_2OH, and

$$f_i(q) = \int d\vec{r} e^{i\vec{q}\cdot\vec{r}} \rho_i(r) = \int_0^\infty dr 4\pi r^2 \rho_i(r) \frac{\sin(qr)}{qr}, \quad (i = H, X) \qquad (33)$$

is the form factor for H atom or CH_2O. Assume the isotropic rotational wave packet of gas phase CH_2OH, and the one-dimensional MXS CD cross section is

$$\Delta\frac{d\sigma}{d\theta}(q) = 2\pi\alpha^6 D_Z(q) \langle s_Z(q)\rangle_{rot}, \qquad (34)$$

$$\langle s_Z(q)\rangle_{rot} = \pm N_{un} \pm \frac{N-1}{N} \left[f_H^2(q) + \frac{\sin(qR_{OH})}{qR_{OH}} f_H(q) f_X(q) \right]. \qquad (35)$$

Note that Eq. (34) and Eq. (35) are similar to the rotational averaged charge scattering x-ray diffraction signal in the independent atom model [43]

$$I_{IAM}(q) \propto \sum_I |f_I(q)|^2 + \sum_{I\neq J} f_I(q) f_J(q) \frac{\sin(qr_{IJ})}{qr_{IJ}}, \qquad (36)$$

where I, J are atomic indexes, $f_I(q)$ is the form factor of the Ith atom, and r_{IJ} is the distance between the Ith atom and Jth atom. The second term in Eq. (36) reflects molecular structural information, which can be interpreted as the superposition of

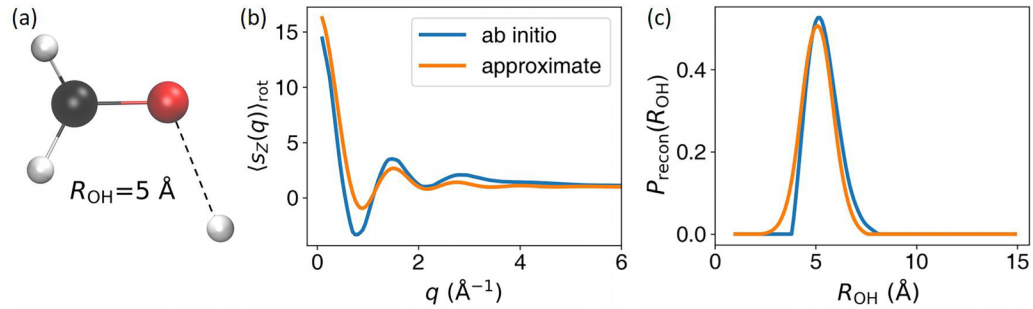

FIG. 6. Rotational averaged spin density for a representative dissociated geometry and retrieved probability density of O–H distance. (a) The representative dissociated geometry with O–H distance $R_{OH} = 5$ Å. Black, red and white spheres represent C, O, and H atoms, respectively. (b) The blue line is the rotational averaged spin density obtained from ab initio calculated MXS CD cross section $\langle s_Z(q)\rangle_{rot} = \frac{1}{2\pi\alpha^6 D_Z(q)}\frac{d\sigma}{d\theta}(q)$ from Eq. (34), and the orange line is calculated by the analytical model derived in Eq. (35). (c) Retrieved probability density of R_{OH} centered at $R_{OH} = 5$ Å.

interference pattern contributed by each pair of atoms. Likewise, the MXS CD signal can be regarded as the interference pattern by the CH_2O and dissociated H atom, and the spacing of fringes is $\Delta q \sim \frac{1}{R_{OH}}$, due to the factor $\frac{\sin(qR_{OH})}{qR_{OH}}$. Δq decreases with the dissociation of CH_2OH molecule, and goes beyond resolution with CH_2OH dissociation.

Equation (34) can be analytically reversed to solve R_{OH} from MXS CD signal, using the following orthogonal property:

$$\int_0^{+\infty} dq q^2 \frac{\sin(qR_{OH})}{qR_{OH}} \frac{\sin(qR'_{OH})}{qR'_{OH}} = \frac{1}{2R_{OH}R'_{OH}} \int_0^{+\infty} dq[\cos(qR_{OH} - qR'_{OH}) - \cos(qR_{OH} + qR'_{OH})]$$
$$= \frac{\pi}{2R_{OH}^2}\delta(R_{OH} - R'_{OH}), \quad (R_{OH} > 0, R'_{OH} > 0), \tag{37}$$

where we have used the formula

$$\int_0^{+\infty} dq \cos(qx) = \frac{1}{2}\int_{-\infty}^{+\infty} dq \cos(qx) = \frac{1}{4}\int_{-\infty}^{+\infty} dq(e^{iqx} + e^{-iqx}) = \pi\delta(x). \tag{38}$$

So the O–H distance can be retrieved from Eq. (34) by (for spin-up molecules)

$$\frac{2R^2}{\pi}\int_0^{+\infty} dq q^2 \frac{\sin(qR)}{qR}\left[\frac{N}{N-1}\frac{\langle s_Z(q)\rangle_{rot} - N_{un}}{f_H(q)f_X(q)} - \frac{f_H(q)}{f_X(q)}\right] = \delta(R - R_{OH}). \tag{39}$$

We choose a representative dissociated geometry in Fig. 6(a) with $R_{OH} = 5$ Å to validate the analytical model we made in this section to calculate spin density. As shown in Fig. 6(b), the rotational averaged spin density calculated from Eq. (35) is consistent with the *ab initio* calculated result, and the retrieved probability density of O–H distance is centered at $R_{OH} = 5$ Å as shown in Fig. 6(c).

The retrieval method can be generalized to obtain the distribution of R_{OH} for MD trajectories. Define the spin-dependent O–H distance probability $P^{\uparrow}(R_{OH}, t)$ and $P^{\downarrow}(R_{OH}, t)$. After averaging over all MD trajectories, the MXS CD signal is

$$\left\langle \Delta\frac{d\sigma}{d\theta}(q,t)\right\rangle = 2\pi\alpha^6 D_Z \frac{N-1}{N} f_H f_X \int_0^{+\infty} dR_{OH}[P^{\uparrow}(R_{OH},t) - P^{\downarrow}(R_{OH},t)]\frac{\sin(qR_{OH})}{qR_{OH}}. \tag{40}$$

Define $A(q) = \frac{N-1}{Nq}\pi^2\alpha^6 D_Z(q) f_H(q) f_X(q)$ and $\Delta P(R_{OH}, t) = P^{\uparrow}(R_{OH}, t) - P^{\downarrow}(R_{OH}, t)$, and the equation can be expressed as

$$\left\langle \Delta\frac{d\sigma}{d\theta}(q,t)\right\rangle = \frac{2q}{\pi}A(q)\int_0^{+\infty} dR_{OH}\Delta P(R_{OH},t)\frac{\sin(qR_{OH})}{qR_{OH}}. \tag{41}$$

The spatially separated spin distribution, which is given as a function of O–H distance, can be retrieved from the MXS CD intensity by

$$\int_0^{+\infty} dq \frac{q^2}{\frac{2q}{\pi}A(q)} \frac{\sin(qR'_{OH})}{qR'_{OH}}\left\langle \Delta\frac{d\sigma}{d\theta}(q,t)\right\rangle = \int_0^{+\infty} dR_{OH}\Delta P(R_{OH},t)\int_0^{+\infty} dq q^2 \frac{\sin(qR_{OH})}{qR_{OH}}\frac{\sin(qR'_{OH})}{qR'_{OH}}$$
$$= \int_0^{+\infty} dR_{OH}\Delta P(R_{OH},t)\delta(R_{OH} - R'_{OH})\frac{\pi}{2R'^2_{OH}}$$
$$= \Delta P(R'_{OH},t)\frac{\pi}{2R'^2_{OH}}, \tag{42}$$

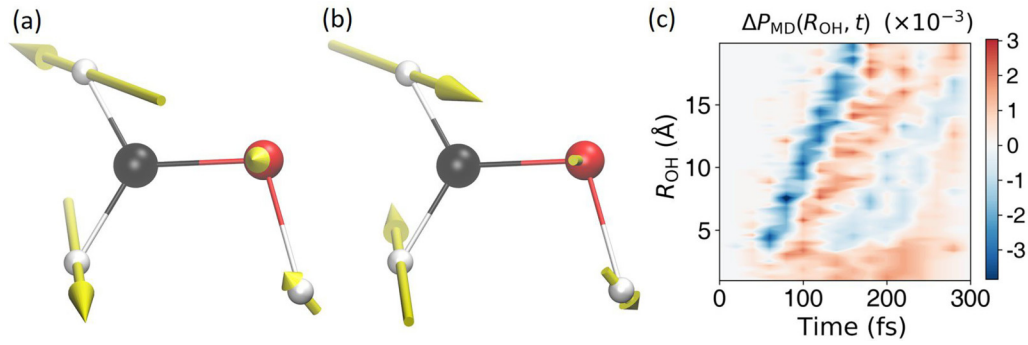

FIG. 7. Berry curvature effect in molecular dynamics (MD) of CH_2OH photodissociation. Representative effective magnetic forces arising from the Berry curvature effect for (a) spin-up and (b) spin-down CH_2OH molecules, which lead to electron-spin-dependent nuclear motions. (c) The difference in probability density $\Delta P_{\mathrm{MD}}(R_{\mathrm{OH}}, t)$ between spin-up and spin-down molecules with O–H distance R_{OH} at time t calculated from MD trajectories.

so

$$\Delta P(R_{\mathrm{OH}}, t) = R_{\mathrm{OH}} \int_0^{+\infty} dq \frac{\sin(qR_{\mathrm{OH}})}{A(q)} \left\langle \Delta \frac{d\sigma}{d\theta}(q, t) \right\rangle. \quad (43)$$

III. RESULTS AND DISCUSSIONS

A. Observing Berry curvature effect in molecular dynamics by ultrafast x-ray diffraction

Representative effective magnetic forces for spin-up and spin-down CH_2OH molecules in CH_2OH photodissociation dynamics are shown in Figs. 7(a) and 7(b). The directions of the effective magnetic forces for spin-up and spin-down molecules are nearly opposite, which can result in the slow-down and speedup of the O–H dissociation for the spin-up and spin-down molecules, respectively, thus the Berry curvature effect can lead to distinct MD trajectories for molecules with opposite initial spin directions. The pair of MD trajectories for identical initial conditions of nuclei but opposite electron spin directions experience nearly opposite effective magnetic fields, and the wave packets for opposite spins are distinguishable in the dissociation process. Figure 7(c) shows the probability difference $\Delta P(R_{\mathrm{OH}}, t)$ between spin-up and spin-down molecules with O–H distance R_{OH} at time t.

To observe the electron-spin-dependent nuclear wave packet motion due to the Berry curvature effect, we calculated the MXS CD signal for CH_2OH molecules based on the MD trajectories,

$$\left\langle \Delta \frac{d\sigma(\vec{q}, t)}{d\Omega} \right\rangle = \frac{\alpha^6}{N_{\mathrm{tr}}} \sum_i \mathrm{Re}[\vec{s}_i^{\uparrow\downarrow}(\vec{q}, t) \cdot \vec{D}(\vec{q})], \quad (44)$$

where i and N_{tr} are the index and total number of MD trajectories, $\vec{s}_i^{\uparrow\downarrow}(\vec{q}, t)$ is the spin density contributed from the ith pair of MD trajectory with opposite spin polarization directions

$$\vec{s}_i^{\uparrow\downarrow}(\vec{q}, t) = p^{\uparrow} \langle \psi^{\uparrow}(\vec{R}_i^{\uparrow}, t) | \hat{\vec{s}}(\vec{q}) | \psi^{\uparrow}(\vec{R}_i^{\uparrow}, t) \rangle + p^{\downarrow} \langle \psi^{\downarrow}(\vec{R}_i^{\downarrow}, t) | \hat{\vec{s}}(\vec{q}) | \psi^{\downarrow}(\vec{R}_i^{\downarrow}, t) \rangle. \quad (45)$$

$\hat{\vec{s}}(\vec{q})$ and $\vec{D}(\vec{q})$ are defined in Sec. II D. We show the simulation result of the MXS CD signal in Fig. 8(a). We assume an isotropic angular distribution for the molecular rotational degrees of freedom and the one-dimensional MXS CD cross section is defined by

$$\Delta \frac{d\sigma}{d\theta}(q) = \int_0^{2\pi} d\phi \Delta \frac{d\sigma}{d\Omega}(q_x = q\cos\phi, q_y = q\sin\phi, q_z = 0). \quad (46)$$

The direction of external magnetic field, defined as Z axis in the laboratory frame, is chosen to be same as the propagation direction of incident x ray. The wavelength of incident x ray is 0.5 Å. As we can see from Fig. 8(a), the intensity of the MXS CD signal shows up within 100 fs, as the Berry curvature effect induces nontrivial spin density.

B. Retrieving the electronic spin density evolution from ultrafast x-ray diffraction

In order to quantitatively retrieve the electronic spin density evolution in the ultrafast photodissociation dynamics of CH_2OH, we establish an analytical model for the MXS CD signal in Sec. II E, which can obtain the distribution of R_{OH} for MD trajectories from MXS CD

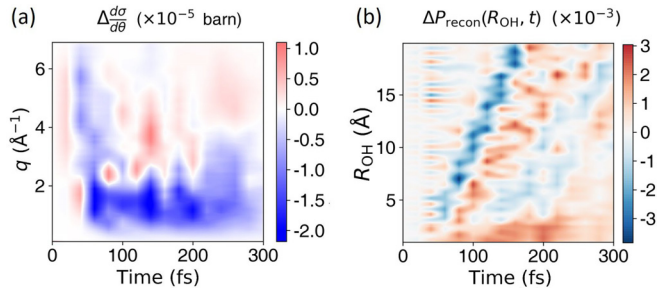

FIG. 8. Simulated ultrafast magnetic x-ray scattering circular dichroism signal of the molecular dynamics trajectories and reconstructed probability density difference for spin-up and spin-down molecules. (a) Ultrafast magnetic x-ray scattering circular dichroism differential cross section $\langle \Delta \frac{d\sigma}{d\theta}(q, t) \rangle$ calculated from the MD trajectories and the corresponding scattered photon counts per second with chosen FEL parameters. Here a 10^{-5} barn cross section corresponds to a photon count rate of $1 \sim 100$ per second. (b) Temporal evolution of the probability density difference $\Delta P_{\mathrm{recon}}(R_{\mathrm{OH}}, t)$ reconstructed from the ultrafast x-ray diffraction signal, which is consistent with Fig. 7(c).

signal. Define the spin-dependent O–H distance probability $P^{\uparrow}(R_{\mathrm{OH}},t)$ and $P^{\downarrow}(R_{\mathrm{OH}},t)$. Denote the probability density of spin-up and spin-down molecules with O–H distance R_{OH} at time t by $P^{\uparrow}(R_{\mathrm{OH}},t)$ and $P^{\downarrow}(R_{\mathrm{OH}},t)$. The difference $\Delta P(R_{\mathrm{OH}},t)=P^{\uparrow}(R_{\mathrm{OH}},t)-P^{\downarrow}(R_{\mathrm{OH}},t)$ indicates the electron-spin-dependent nuclear motion modified by the Berry curvature effect. $\Delta P(R_{\mathrm{OH}},t)$ can be reconstructed from the MXS CD signal by Eq. (43)

$$\Delta P_{\mathrm{recon}}(R_{\mathrm{OH}},t)=R_{\mathrm{OH}}\int dq\frac{\sin(qR_{\mathrm{OH}})}{A(q)}\left\langle\Delta\frac{d\sigma}{d\theta}(q,t)\right\rangle. \quad (47)$$

From the ultrafast MXS CD signal of ultrafast x-ray diffraction shown in Fig. 8(a), $\Delta P_{\mathrm{recon}}(R_{\mathrm{OH}},t)$ can be reconstructed, as shown in Fig. 8(b), and is consistent with Fig. 7(c) calculated directly from the MD trajectories. Thus the ultrafast MXS CD signal can be employed to demonstrate that the dissociation of spin-down molecules is faster than that of spin-up molecules due to the Berry curvature effect.

C. Effect of spin-polarized Boltzmann distribution

In this section, we estimate the spin-polarized Boltzmann distribution resulting from Zeeman energy splitting in the external magnetic field. Denote $p^{\uparrow}$ and $p^{\downarrow}$ as the probabilities of Boltzmann distributions for spin-up and spin-down initial states. In the absence of external magnetic field $p^{\uparrow}=p^{\downarrow}$. For $B=0.1$ T and the temperature $T=300$ K, the Zeeman energy splitting is $\Delta E_{\mathrm{Z}}=\alpha B=0.1/1720\times 1/137\,\mathrm{au}=4.25\times10^{-7}\,\mathrm{au}$, and $k_{\mathrm{B}}T=1.38\times10^{-23}\,\mathrm{J/K}\times 300\,\mathrm{K}=9.51\times10^{-4}\,\mathrm{au}$, where k_{B} is the Boltzmann constant, so

$$|p^{\uparrow}-p^{\downarrow}|=\frac{1-e^{-\Delta E_{\mathrm{Z}}/k_{\mathrm{B}}T}}{1+e^{-\Delta E_{\mathrm{Z}}/k_{\mathrm{B}}T}}\approx\frac{\Delta E_{\mathrm{Z}}}{2k_{\mathrm{B}}T}=\frac{4.25\times10^{-7}\,\mathrm{au}}{2\times9.51\times10^{-4}\,\mathrm{au}}\approx2\times10^{-4}. \quad (48)$$

The MXS signal reflecting the Berry curvature effect corresponds to $p^{\uparrow}=p^{\downarrow}=\frac{1}{2}$ in Eq. (45). The spin density signal originated from Boltzmann distribution also leads to the dominant noise, whose magnitude can be estimated by

$$\Delta\frac{d\sigma^{\mathrm{noise}}(\vec{q},t)}{d\Omega}\approx|p^{\uparrow}-p^{\downarrow}|\alpha^{6}\left\langle\mathrm{Re}[\langle\psi^{\uparrow}(\vec{R}^{\uparrow}(t))|\hat{\vec{s}}|\psi^{\uparrow}(\vec{R}^{\uparrow}(t))\rangle\cdot\vec{D}(\vec{q})]\right\rangle_{\downarrow}. \quad (49)$$

From Eq. (48), we have $|p^{\uparrow}-p^{\downarrow}|\approx2\times10^{-4}$, and $\alpha^{6}\langle\mathrm{Re}[\langle\psi^{\uparrow}(\vec{R}^{\uparrow}(t))|\hat{\vec{s}}|\psi^{\uparrow}(\vec{R}^{\uparrow}(t))\rangle\cdot\vec{D}(\vec{q})]\rangle_{\downarrow}$ is the averaged spin density for spin-down MD trajectories. As shown in Fig. 9, the signal originated from Boltzmann distribution is $\sim10^{-7}$ barn, and is $\sim10^{-2}$ smaller than the MXS CD signal caused by the Berry curvature effect, which is $\sim10^{-5}$ barn as shown in Fig. 8(a).

D. Scattered x-ray photon counts estimation and signal contrast

The scattered x-ray photon counts of the MXS CD signal are calculated from the cross section under feasible experimental conditions of free electron laser (FEL) [44,45]. The

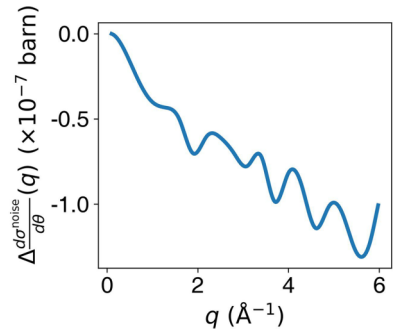

FIG. 9. Diffraction noise signal caused by Boltzmann distribution $\Delta\frac{d\sigma^{\mathrm{noise}}}{d\theta}(q)$ is in the 10^{-7} barn order of magnitude. The MXS signal noise is calculated from the MD trajectories, and the time instant corresponding to maximum noise signal is shown.

total number of scattered photons N_{total} is

$$N_{\mathrm{total}}=N_{\mathrm{MXS}}N_{\mathrm{pulse}}N_{\mathrm{mol}}, \quad (50)$$

where N_{MXS} is the number of scattered photons for one incident XFEL pulse and one target molecule, N_{pulse} is the number of incident XFEL pulses and N_{mol} is the number of target molecules. First, we have

$$N_{\mathrm{MXS}}=\sigma\frac{N_{\gamma}}{d^{2}}, \quad (51)$$

where σ is the MXS cross section, N_{γ} is the number of photons per pulse, d is the photon source size, and

$$N_{\mathrm{mol}}=\rho d^{2}L, \quad (52)$$

where ρ is the molecular density of gas jet, $d^{2}L$ is the interaction volume and L is the gas jet size, and

$$N_{\mathrm{pulse}}=\nu T, \quad (53)$$

where ν is the repetition rate and T is the time of measurement. Using the XFEL parameters of photon number per FEL pulse $N_{\gamma}=10^{12}$, repetition rate of the FEL pulses $\nu=1$ MHz, the molecular density of gas jet is assumed to be $\rho=10^{12}\sim10^{14}\,\mathrm{cm}^{-3}$ at the interaction region, and the gas jet size $L=1$ mm, the scattered photon number per second for $\sigma=10^{-5}$ barn is

$$N_{\mathrm{total}}=\sigma N_{\gamma}\rho L\nu T\approx10^{-5}\,\mathrm{barn}\times10^{12}\times10^{12}\,\mathrm{cm}^{-3}\times1\,\mathrm{mm}\times1\,\mathrm{MHz}\times1\,\mathrm{s}=1 \quad (54)$$

when $\rho=10^{12}\,\mathrm{cm}^{-3}$ and $N_{\mathrm{total}}=100$ when $\rho=10^{14}\,\mathrm{cm}^{-3}$. Practically, repeated experiments are necessary to obtain the circular dichroism signals, in order to eliminate the effect of the intensity fluctuations of the FEL pulses in the self-amplified spontaneous emission (SASE) [44] or the seeded regime [46].

The contrast of the MXS CD signal is defined as $\frac{\sigma_{\mathrm{L}}-\sigma_{\mathrm{R}}}{\sigma_{\mathrm{L}}+\sigma_{\mathrm{R}}}$, where $\sigma_{\mathrm{L/R}}$ is the scattering cross section of left-handed/right-handed circularly polarized incident x ray. $\sigma_{\mathrm{L}}+\sigma_{\mathrm{R}}$ is dominantly contributed by the charge scattering signal of ultrafast x-ray diffraction, and the order of magnitude can be directly estimated by Thomson scattering cross section

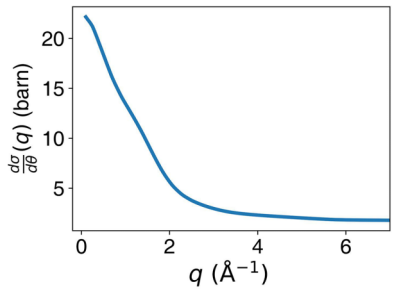

FIG. 10. *Ab initio* calculated charge scattering cross section for the molecular geometry shown in Fig. 6(a).

formula [36]

$$\sigma_{\text{charge}}(\vec{q}) = \alpha^4 |\vec{e}_1 \cdot \vec{e}_2^*|^2 |f(\vec{q})|^2, \tag{55}$$

where α^4 corresponds the cross section of about 0.08 barn, and the form factor $f(\vec{q})$, when $\vec{q} = 0$, is equal to the number of electrons in CH_2OH molecule. Thus apart from the $|\vec{e}_1 \cdot \vec{e}_2^*|^2$ polarization factor, the charge scattering cross section is

$$\sigma_{\text{charge}}(\vec{q} = 0) \approx 0.08\,\text{barn} \times 17^2 \approx 23\,\text{barn}, \tag{56}$$

which is on the order of 10 barn, consistent with the charge scattering cross section of a representative CH_2OH geometry shown in Fig. 10. Thus the contrast of the MXS CD signal is about 10^{-6}. Similar contrast level was also adopted in other works, such as in the probing of the electronic coherence using twisted x-ray diffraction [47].

IV. CONCLUSION

To summarize, we have proposed an experimental scheme for the observation of nontrivial Berry curvature effect in molecular dynamics. We have simulated the MXS CD signal of the electron-spin-dependent photodissociation of CH_2OH, and reconstructed the probability density difference between spin-up and spin-down molecules, which demonstrates that the dissociation of spin-down molecules is faster than that of spin-up molecules in the presence of the effective magnetic field corresponding to the Berry curvature. Our work also opens a window to the observation and study of the Berry curvature effect in other systems of physics and chemistry [48–51].

ACKNOWLEDGMENTS

We thank R. J. Dwayne Miller, Zhaoheng Guo, and Zunqi Li for helpful discussions. This work has been supported by the National Key R&D Program (Grant No. 2023YFA1406801), National Natural Science Foundation of China (Grants No. 92250303, No. 12234002, No. 12174009, and No. 11974031), Innovation Program for Quantum Science and Technology (Grant No. 2021ZD0301702), Beijing Natural Science Foundation (Grant No. Z220008).

[1] M. V. Berry, Quantal phase factors accompanying adiabatic changes, Proc. R. Soc. Lond., Ser. A, Math. Phys. Eng. Sci. **392**, 45 (1984).
[2] B. A. Bernevig and T. L. Hughes, *Topological Insulators and Topological Superconductors* (Princeton University Press, Princeton, 2013).
[3] F. Liu and K. Wakabayashi, Novel topological phase with a zero Berry curvature, Phys. Rev. Lett. **118**, 076803 (2017).
[4] F. D. M. Haldane, Nobel lecture: Topological quantum matter, Rev. Mod. Phys. **89**, 040502 (2017).
[5] Z. F. Marlan, *Quantum Hall Effects: Field Theoretical Approach and Related Topics* (World Scientific Press, Singapore, 2008).
[6] F. D. M. Haldane, Berry curvature on the Fermi surface: Anomalous Hall effect as a topological Fermi-liquid property, Phys. Rev. Lett. **93**, 206602 (2004).
[7] P. Bruno, V. K. Dugaev, and M. Taillefumier, Topological Hall effect and Berry phase in magnetic nanostructures, Phys. Rev. Lett. **93**, 096806 (2004).
[8] D. Xiao, M.-C. Chang, and Q. Niu, Berry phase effects on electronic properties, Rev. Mod. Phys. **82**, 1959 (2010).
[9] C. A. Mead, The geometric phase in molecular systems, Rev. Mod. Phys. **64**, 51 (1992).
[10] P. Garcia-Fernandez, I. B. Bersuker, and J. E. Boggs, Lost topological (Berry) phase factor in electronic structure calculations. example: The ozone molecule, Phys. Rev. Lett. **96**, 163005 (2006).
[11] D. Yuan, Y. Guan, W. Chen, H. Zhao, S. Yu, C. Luo, Y. Tan, T. Xie, X. Wang, Z. Sun, D. Zhang, and X. Yang, Observation of the geometric phase effect in the H + HD → H_2+ D reaction, Science **362**, 1289 (2018).
[12] J. C. Juanes-Marcos, S. C. Althorpe, and E. Wrede, Theoretical study of geometric phase effects in the hydrogen-exchange reaction, Science **309**, 1227 (2005).
[13] T. Culpitt, L. D. M. Peters, E. I. Tellgren, and T. Helgaker, *Ab initio* molecular dynamics with screened Lorentz forces. I. calculation and atomic charge interpretation of Berry curvature, J. Chem. Phys. **155**, 024104 (2021).
[14] L. Yin and C. A. Mead, Magnetic screening of nuclei by electrons as an effect of geometric vector potential, J. Chem. Phys. **100**, 8125 (1994).
[15] J. Subotnik, G. Miao, N. Bellonzi, H.-H. Teh, and W. Dou, A demonstration of consistency between the quantum classical liouville equation and Berry's phase and curvature, J. Chem. Phys. **151**, 074113 (2019).
[16] L. D. M. Peters, T. Culpitt, E. I. Tellgren, and T. Helgaker, Berry population analysis: Atomic charges from the berry curvature in a magnetic field, J. Chem. Theory Comput. **19**, 1231 (2023).
[17] Y. Wu and J. E. Subotnik, Electronic spin separation induced by nuclear motion near conical intersections, Nature Commun. **12**, 700 (2021).
[18] X. Bian, Y. Wu, H.-H. Teh, Z. Zhou, H.-T. Chen, and J. E. Subotnik, Modeling nonadiabatic dynamics with degenerate electronic states, intersystem crossing, and spin separation: A key goal for chemical physics, J. Chem. Phys. **154**, 110901 (2021).
[19] Z. Tao, T. Qiu, and J. E. Subotnik, Symmetric post-transition state bifurcation reactions with Berry pseudomagnetic fields, J. Phys. Chem. Lett. **14**, 770 (2023).
[20] Y. Wu, G. Miao, and J. E. Subotnik, Chemical reaction rates for systems with spin–orbit coupling and an odd number of

electrons: Does Berry's phase lead to meaningful spin-dependent nuclear dynamics for a two state crossing? J. Phys. Chem. A **124**, 7355 (2020).

[21] C. L. Malbon and D. R. Yarkony, Multistate, multichannel coupled diabatic state representations of adiabatic states coupled by conical intersections. CH_2OH photodissociation, J. Chem. Phys. **146**, 134302 (2017).

[22] C. L. Malbon and D. R. Yarkony, Nonadiabatic photodissociation of the hydroxymethyl radical from the 2^2A state. surface hopping simulations based on a full nine-dimensional representation of the 1, 2, 3^2A potential energy surfaces coupled by conical intersections, J. Phys. Chem. A **119**, 7498 (2015).

[23] L. Feng, X. Huang, and H. Reisler, Photodissociative spectroscopy of the hydroxymethyl radical (CH_2OH) in the 3s and $3p_x$ states, J. Chem. Phys. **117**, 4820 (2002).

[24] P. W. Abegg, *Ab initio* calculation of spin-orbit coupling constants for gaussian lobe and gaussian-type wave functions, Mol. Phys. **30**, 579 (1975).

[25] P. A. Malmqvist, A. Rendell, and B. O. Roos, The restricted active space self-consistent-field method, implemented with a split graph unitary group approach, J. Phys. Chem. **94**, 5477 (1990).

[26] T. Culpitt, L. D. M. Peters, E. I. Tellgren, and T. Helgaker, Analytic calculation of the Berry curvature and diagonal Born–Oppenheimer correction for molecular systems in uniform magnetic fields, J. Chem. Phys. **156**, 044121 (2022).

[27] G. Miao, N. Bellonzi, and J. Subotnik, An extension of the fewest switches surface hopping algorithm to complex Hamiltonians and photophysics in magnetic fields: Berry curvature and magnetic forces, J. Chem. Phys. **150**, 124101 (2019).

[28] K. Andersson, F. Aquilante, M. Barysz, A. Bernhardsson, M. R. A. Blomberg *et al.*, Molcas, version py2.15, a package of *ab initio* programs, see https://www.molcas.org.

[29] X. Bian, Y. Wu, H.-H. Teh, and J. E. Subotnik, Incorporating Berry force effects into the fewest switches surface-hopping algorithm: Intersystem crossing and the case of electronic degeneracy, J. Chem. Theory Comput. **18**, 2075 (2022).

[30] J. C. Tully, Molecular dynamics with electronic transitions, J. Chem. Phys. **93**, 1061 (1990).

[31] W. Schülke, *Electron Dynamics by Inelastic X-Ray Scattering* (Oxford University Press, Oxford, 2007).

[32] M. Blume, Magnetic scattering of x rays (invited), J. Appl. Phys. **57**, 3615 (1985).

[33] X. Mi, M. Zhang, and Z. Li, Ultrafast X-ray diffraction probe of coherent spin-state dynamics in molecules, J. Phys. Chem. Lett. **15**, 681 (2024).

[34] P. M. Platzman and N. Tzoar, Magnetic scattering of x rays from electrons in molecules and solids, Phys. Rev. B **2**, 3556 (1970).

[35] H. Ohsumi and T.-h. Arima, Novel insight into structural magnetism by polarized synchrotron X-ray scattering, Adv. Phys. X **1**, 128 (2016).

[36] R. Santra, Concepts in x-ray physics, J. Phys. B **42**, 169801 (2009).

[37] R. Santra, G. Dixit, and J. M. Slowik, "Comment on: How to observe coherent electron dynamics directly", Phys. Rev. Lett. **113**, 189301 (2014).

[38] D. Popova-Gorelova, Imaging electron dynamics with ultrashort light pulses: A theory perspective, Appl. Sci. **8**, 318 (2018).

[39] X. Mu, M. Zhang, J. Feng, H. Yang, N. Medvedev, X. Liu, L. Yang, Z. Wu, H. Xu, and Z. Li, Identification of the decay pathway of photoexcited nucleobases, Ultrafast Science **3**, 0015 (2023).

[40] J. Yang, X. Zhu, J. P. F. Nunes, J. K. Yu, R. M. Parrish, T. J. A. Wolf, M. Centurion, M. Gühr, R. Li, Y. Liu, B. Moore, M. Niebuhr, S. Park, X. Shen, S. Weathersby, T. Weinacht, T. J. Martinez, and X. Wang, Simultaneous observation of nuclear and electronic dynamics by ultrafast electron diffraction, Science **368**, 885 (2020).

[41] J. Yang, X. Zhu, T. Wolf, Z. Li, J. P. F. Nunes, R. Coffee, J. P. Cryan, M. Gühr, K. Hegazy, T. F. Heinz, K. Jobe, R. K. Li, X. Z. Shen, T. Veccione, S. Weathersby, K. J. Wilkin, C. Yoneda, Q. Zheng, T. J. Martinez, M. Centurion, and X. Wang, Imaging CF_3I conical intersection and photodissociation dynamics with ultrafast electron diffraction, Science **361**, 64 (2018).

[42] H. J. Werner, P. J. Knowles, G. Knizia, R. Lindh, F. R. Manby, M. Schütz *et al.*, Molpro, version 2019.2, a package of *ab initio* programs, see https://www.molpro.net.

[43] J. M. Budarz, M. P. Minitti, D. V. Cofer-Shabica, B. Stankus, A. Kirrander, J. B. Hastings, and P. M. Weber, Observation of femtosecond molecular dynamics via pump-probe gas phase x-ray scattering, J. Phys. B **49**, 034001 (2016).

[44] P. Emma, R. Akre, J. Arthur, R. Bionta, C. Bostedt, J. Bozek, A. Brachmann, P. Bucksbaum, R. Coffee, F.-J. Decker, Y. Ding, D. Dowell, S. Edstrom, A. Fisher, J. Frisch, S. Gilevich, J. Hastings, G. Hays, P. Hering, Z. Huang *et al.*, First lasing and operation of an ångstrom-wavelength free-electron laser, Nature Photon. **4**, 641 (2010).

[45] P. G. O'Shea and H. P. Freund, Free-electron lasers: Status and applications, Science **292**, 1853 (2001).

[46] L. Giannessi, M. Artioli, M. Bellaveglia, F. Briquez, E. Chiadroni, A. Cianchi, M. E. Couprie, G. Dattoli, E. Di Palma, G. Di Pirro, M. Ferrario, D. Filippetto, F. Frassetto, G. Gatti, M. Labat, G. Marcus, A. Mostacci, A. Petralia, V. Petrillo, L. Poletto *et al.*, High-order-harmonic generation and superradiance in a seeded free-electron laser, Phys. Rev. Lett. **108**, 164801 (2012).

[47] H. Yong, J. R. Rouxel, D. Keefer, and S. Mukamel, Direct monitoring of conical intersection passage via electronic coherences in twisted x-ray diffraction, Phys. Rev. Lett. **129**, 103001 (2022).

[48] E. Cohen, H. Larocque, F. Bouchard, F. Nejadsattari, Y. Gefen, and E. Karimi, Geometric phase from Aharonov–Bohm to Pancharatnam–Berry and beyond, Nature Rev. Phys. **1**, 437 (2019).

[49] A. Kuppermann and Y.-S. M. Wu, The geometric phase effect shows up in chemical reactions, Chem. Phys. Lett. **205**, 577 (1993).

[50] D. T. Son and N. Yamamoto, Berry curvature, triangle anomalies, and the chiral magnetic effect in Fermi liquids, Phys. Rev. Lett. **109**, 181602 (2012).

[51] M. V. Berry and P. Shukla, Geometric phase curvature for random states, J. Phys. A **51**, 475101 (2018).